Quantification of 3D Musculoskeletal CT Image-Based Biomarkers in the Lumbar Spine: Application in Metastatic Prostate Cancer

Saleh Tabatabaei[1,2], Tayler D. Ross[1,2], Urban Emmenegger[1,2], Cari M. Whyne[1,2], and Michael Hardisty[1,2]

[1] Sunnybrook Research Institute, Toronto, Canada
[2] University of Toronto, Toronto, Canada

Abstract. Osteosarcopenia, characterized by concurrent deterioration of bone and muscle, is increasingly recognized as a major contributor to frailty, fractures, and mortality, particularly in prostate cancer. However, quantitative longitudinal assessment of osteosarcopenia remains limited by existing manual methods based on 2D analysis at a single time point, which are impractical for large-scale monitoring and cannot detect subtle changes over time due to slice-selection variability. This study introduces an AI-enabled pipeline to quantify musculoskeletal (MSK) changes from 3D serial CT scans in prostate cancer. The pipeline integrates deep learning–based vertebrae detection and 3D vertebral body and psoas muscle segmentation. Lumbar vertebral bone density, psoas muscle volume and density were retrospectively quantified from 5,966 CT scans acquired from a cohort of 916 metastatic prostate cancer patients (2008–2024). The pipeline demonstrated strong agreement with a manually contoured test set for vertebral density (R^2=0.874-0.986), psoas density (R^2=0.955), and psoas volume (R^2=0.830). In repeated short-interval scans, the proposed 3D biomarkers showed higher reliability than conventional 2D measurements for psoas density (ICC(3,1)=0.86 vs. 0.72) and psoas volume versus cross-sectional area (ICC(3,1)=0.94 vs. 0.87). Longitudinal mixed-effects modeling showed that declining muscle and bone biomarkers were associated with increasing lumbar metastatic burden (p<0.05). The combined muscle model explained the greatest proportion of variance (marginal R^2=0.424). These findings demonstrate that automated 3D CT-based biomarkers provide reliable and clinically meaningful measures of progressive MSK decline. This framework enables scalable opportunistic monitoring of osteosarcopenia and may support earlier identification of patients at risk for treatment-related deterioration, metastatic progression, and fracture.

Keywords: Osteosarcopenia · Deep Learning · Musculoskeletal Biomarkers · Longitudinal CT Imaging · Prostate Cancer · Opportunistic Imaging

1 Introduction

Musculoskeletal (MSK) health is an increasing concern as the population ages. With advancing age, individuals experience progressive declines in bone density

and in muscle quality, quantity, and strength [1]. This deterioration can result in osteosarcopenia, a progressive condition characterized by the coexistence of osteopenia/osteoporosis (reduced bone density) and sarcopenia (loss of muscle mass, strength, and function) [2]. Individuals with osteosarcopenia have higher rates of fractures [1, 3], falls [1, 3], hospitalizations [1], and mortality [1, 4].

MSK health in cancer patients has gained importance as survival improves (*e.g.*, secondary to advances in immunotherapy and hormone therapy). Osteosarcopenia is common in prostate cancer. Both active disease and its treatments (*e.g.*, androgen deprivation therapy) have severe consequences on bone and muscle, leading to frailty, fractures, hospital readmissions, and reduced independence [5, 6]. MSK changes occur progressively over many years: Skeletal muscle mass declines by approximately 1–4% per year [7], while bone mineral density (BMD) decreases by about 2–5% annually [8]. However, quantitative clinical assessment of osteosarcopenia in prostate cancer remains limited by manual two-dimensional (2D) methods impractical for large-scale longitudinal monitoring.

Recent studies have applied deep learning to automate MSK measurements from diagnostic computed tomography (CT). Choi et al. trained an nnU-Net to segment the psoas muscle on axial CT slices with good performance (Dice similarity coefficient[DSC]=0.927), however, results suggested that volumetric measurements may be more accurate [9]. Rozynek et al. reviewed deep learning applications in sarcopenia imaging, noting that most approaches used convolutional neural networks (CNNs) on axial CT images to extract single-slice L3 cross-sectional measurements (*e.g.*, skeletal muscle area or psoas muscle index) [10]. Beetz et al. used a U-Net model to compute the psoas muscle index and mean muscle density at L3 [11], while Lee et al.'s L3SEG-net (YOLOv3+FCN) automatically selected the L3 slice, measuring abdominal muscle cross-sectional area in a single step [12]. These methods, while successful for analyzing single time points, are not well-suited to assessing progression in serial imaging. BMD assessment faces similar limitations. Although dual-energy X-ray absorptiometry (DXA) remains the clinical standard of care, it is primarily optimized for single-time-point evaluation and provides a 2D projection of a three-dimensional (3D) structure, which is susceptible to artifacts from fractures, orthopedic implants, metastatic lesions, and changes in patient positioning [13, 14].

Prior work has focused on single-slice measurements, which are sensitive to errors from image-plane selection and patient positioning. Even small deviations in slice location can substantially alter cross-sectional area measurements and limit the reliability of longitudinal progression tracking [15]. To address these limitations, we propose an automated pipeline to quantify small scan-to-scan changes in 3D biomarkers from opportunistic serial CT scans: lumbar vertebral bone density, and psoas muscle volume and density. The main contributions are as follows: (1) Development of an automated pipeline of 3D MSK image-based biomarkers (vertebral bone density, psoas muscle volume, and muscle density) that quantify changes in muscle and bone health from serial imaging. (2) Demonstration that the pipeline has state-of-the-art reliability for the assessment of MSK biomarkers, enabling robust osteosarcopenia progression assessment. (3)

Establishing clinical relevance by showing that biomarker changes are associated with cancer progression and increasing metastatic involvement over time.

2 Materials and Methods

2.1 Musculoskeletal biomarker extraction pipeline

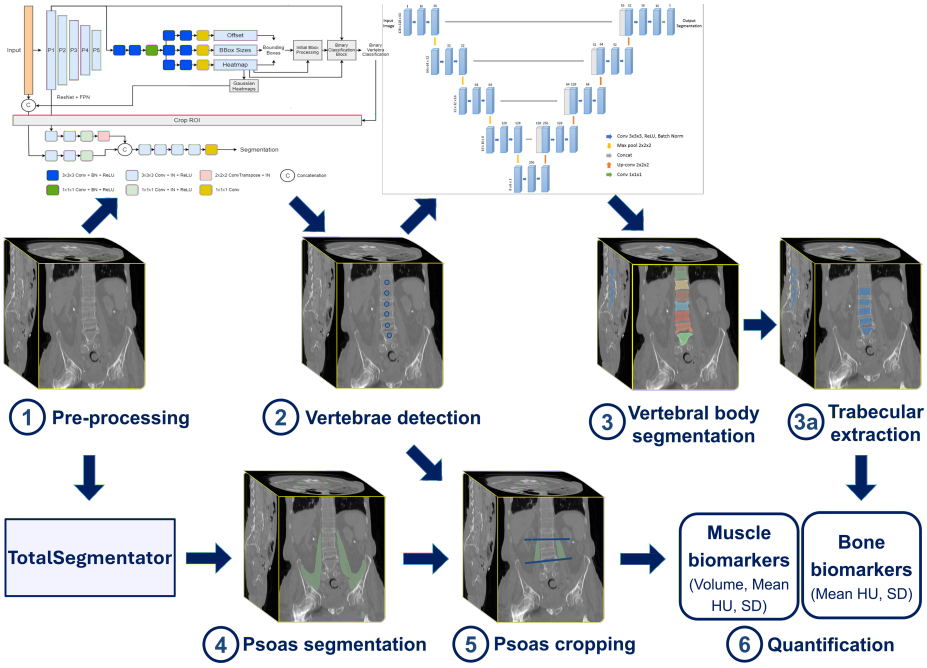

Fig. 1. Overview of the automated multi-stage pipeline for MSK biomarker extraction from 3D CT scans: pre-processing (1), lumbar vertebrae detection using VertDetect [16] (2), vertebral body segmentation using a 3D U-Net [17] (3), trabecular centrum isolation (3a), psoas muscle segmentation using TotalSegmentator [18] (4), psoas cropping based on vertebral centroid landmarks (5), and biomarker quantification (6), including vertebral trabecular density (HU), psoas muscle volume (cm^3) and density (HU).

An automated pipeline was developed to extract MSK imaging biomarkers from 3D Digital Imaging and Communications in Medicine (DICOM) CT scans using medical image analysis and deep learning–based detection and segmentation (Figure 1). The pipeline (Python 3.9.13) comprised the following stages:

1. Pre-processing: Raw DICOM CT scans were converted to Nearly Raw Raster Data (NRRD) format, and DICOM metadata were captured (3D Slicer 5.6). CT volumes (DICOM series) were selected using image metadata (DICOM

tags); only image volumes containing the entire lumbar spine were accepted. Image resampling was applied (if needed) to a 1-mm isotropic voxel size.

2. Vertebrae detection: Lumbar vertebrae (L1–L5) were detected, labeled, segmented, and their centroids predicted using a deep learning model previously developed in our laboratory, VertDetect [16]. The model is a 3D CNN with a ResNet-50 and Feature Pyramid Network backbone, a Graph Convolutional Network layer for refined vertebral labeling, and multiple output heads (vertebrae detection, segmentation, and centroid heatmap prediction). Post-processing used Euclidean distance constraints to correct localization failures. The network was trained on the VerSe 2019 and 2020 datasets [19, 20] and achieved DSCs of 0.88 and 0.87 on their respective test sets.[3]

3. Segmentation of lumbar vertebral bodies: Individual vertebral bodies (centered on the centroid locations identified in stage 2) were segmented using a 6-layer 3D U-Net with 32 base filters, trained to segment metastatically involved vertebral bodies [17]. The model was trained on 530 training and 130 validation segmentations.[4] Each vertebral body segmentation was eroded by 20% to isolate the trabecular centrum and exclude the cortical shell.

4. Psoas muscle segmentation: The iliopsoas muscles were segmented using TotalSegmentator [18], a tool designed for robust segmentation of major anatomical structures in CT.

5. Cropping of psoas muscle segmentation: The segmented psoas muscles were cropped to an anatomically consistent region spanning the L2/L3 and L4/L5 junctions using planes perpendicular to the inter-centroid vectors of adjacent vertebrae. This region of the psoas was selected due to its multiple bony attachments, which maintain a stable spatial relationship between the muscle and the lumbar vertebrae. Let $\mathbf{c}_{L_i} \in R^3$ denote the centroid of vertebra L_i derived from stage 2. The cropped psoas region was defined as:

$$M_{crop} = \left\{ \mathbf{x} \in M_{psoas} \mid \mathbf{n}_{23}^{\top}(\mathbf{x} - \mathbf{m}_{23}) \geq 0 \wedge \mathbf{n}_{45}^{\top}(\mathbf{x} - \mathbf{m}_{45}) \leq 0 \right\}, \qquad (1)$$

where $\mathbf{n}_{ij} = (\mathbf{c}_{L_j} - \mathbf{c}_{L_i})/\|\mathbf{c}_{L_j} - \mathbf{c}_{L_i}\|$ and $\mathbf{m}_{ij} = (\mathbf{c}_{L_i} + \mathbf{c}_{L_j})/2$. After cropping, the largest connected components were retained for biomarker calculation.

6. Quantification of musculoskeletal biomarkers: For bone assessment, the mean and standard deviation of the density (measured in Hounsfield Units [HU]) of the vertebral body trabecular centrum (L1–L5) were calculated. For muscle assessment, biomarkers included total volume of the cropped psoas muscles (in cm^3) and density mean and standard deviation (in HU). A 5% correction factor was applied to the psoas muscle volume to account for systematic underestimation by TotalSegmentator relative to manual annotations.

2.2 Experiment

Study design The study was a retrospective analysis of 916 male patients, including all advanced prostate cancer patients considered for systemic therapy

[3] Training was performed using the AdamW optimizer (learning rate = 10^{-4}, batch size = 4) for 1500 epochs on four NVIDIA Tesla V100 GPUs.

[4] Training was done using the AdamW optimizer (learning rate = 10^{-4}) for 200 epochs.

at Sunnybrook Health Sciences Centre between January 2008 and December 2024 (Sunnybrook Research Ethics Board #1801). The average age at the first CT scan was 72.6 years (range: 41–98 years). Patients underwent periodic CT scans (1–3 per year) to monitor disease progression. All imaging data were retrieved, yielding a total of 14,060 scans, each representing a separate study. These CT scans were used opportunistically in this study to quantify longitudinal changes in MSK health associated with the progression of osteosarcopenia.

Imaging study filtering Using DICOM metadata, scans were filtered based on the following criteria: modality must be CT, and the CT reconstruction must contain the entire lumbar spine, resulting in 5,966 scans remaining. Among these, patients had between 1 and 34 scans (mean = 6.5 scans) and a mean follow-up period of 1,369 days (range = 0–5,280 days); 75% of the cohort had more than two scans, facilitating longitudinal tracking of MSK health.

All CT imaging was acquired under routine imaging protocols with weekly phantom calibration. Scans were performed on GE Medical Systems (2008–2022; n = 5,035; LightSpeed VCT and BrightSpeed) and Siemens Healthineers (2022–2024; n = 931; SOMATOM Force) scanners. In-plane pixel spacing ranged from 0.70 to 0.98 mm, and slice thickness ranged from 1 to 5 mm. Reconstructions were generated using soft-tissue kernels (GE STANDARD and Siemens Br40), with tube voltages predominantly set at 120 kVp for GE and 100 kVp for Siemens acquisitions. Intravenous (IV) contrast enhancement (with possible oral contrast administration) was used in 5,367 studies.

2.3 Statistical analysis and pipeline evaluation

Pipeline performance A subset of manually annotated scans was selected from the larger cohort to establish the ground truth for evaluation, comprising 40 scans of trabecular bone and 50 of psoas muscle. Scans were chosen to capture variability in scanner vendor, IV contrast administration, scan type, and patient age. Manual segmentations were performed by orthopedic surgery resident T.D.R. and PhD student S.T. using the same processing procedures as the pipeline, ensuring spatial consistency. 3D biomarkers extracted from the manual segmentations were compared with corresponding automated outputs.

Reliability was assessed through scan-to-scan variability. In accordance with prior literature, 2D psoas muscle cross-sectional area (cm^2) and mean muscle attenuation (HU) were measured on axial CT at the centroid of the L3 vertebra and compared with the corresponding 3D muscle biomarkers. Reliability was assessed using the intraclass correlation coefficient (ICC(3,1)) in 40 paired CTs acquired within a two-day interval, during which physiological changes in the biomarkers are expected to be negligible; therefore, observed differences were attributed to measurement variability, providing an estimate of the precision of detecting subtle longitudinal changes.

Longitudinal association with metastatic involvement To demonstrate the potential clinical utility of the image-based biomarkers, we examined their

longitudinal association with metastatic involvement of the lumbar spine using repeated CT scans. Patients with more than two CT examinations and a minimum interval of three months between the first and last scan were included to reduce temporal redundancy. The final cohort consisted of 725 patients with 4,905 scans from which biomarkers were extracted. For each scan, radiology reports and corresponding CT images were manually reviewed by an orthopedic surgery resident (T.D.R.) to determine metastatic involvement of the lumbar vertebral bodies (L1–L5). The number of metastatic vertebral levels identified in each scan served as the outcome variable. To ensure that the bone biomarker reflected systemic bone density, vertebral bodies with metastatic involvement were excluded from analyses. Imaging biomarkers (psoas muscle density, psoas muscle volume, and the mean density of lumbar vertebral bodies without metastatic involvement) were included as fixed-effect predictors. All biomarker values were standardized (z-scored) within their respective analytic subsets to ensure comparability of effect sizes and to improve numerical stability. A linear mixed-effects model was used to account for within-patient and between-patient variability. Five models were fitted to evaluate combinations of biomarkers: (1) muscle density only; (2) muscle volume only; (3) muscle density and muscle volume; (4) bone density only; and (5) combined muscle and bone biomarkers. Models involving bone density were restricted to scans from patients with at least one lumbar vertebral level without metastatic involvement at their final examination, yielding a subset of 577 patients with 3,448 scans.

All models were fitted using Restricted Maximum Likelihood. For each model, fixed-effect coefficients (β) with corresponding p-values and 95% confidence intervals were estimated. To quantify variance explained by biomarkers alone and by the full model including patient-level heterogeneity, marginal and conditional R^2 values were calculated. Patient-level random-effect variance was also reported to describe between-patient differences in baseline metastatic burden.

3 Results

3.1 Pipeline performance

The pipeline successfully processed 99.5% (5,937/5,966) of scans. The vertebrae detection failure rate was 1.59% (473/29,830 vertebrae), resulting in complete biomarker quantification in 94.7% (5,650/5,966) of scans. The presence of spinal hardware, bone cement, and fractures precluded quantification of level-specific biomarkers in a subset of scans.

In repeated-scan analysis, 3D biomarkers demonstrated higher reliability than prior 2D methods (Table 1). Psoas muscle mean density had an ICC(3,1) of 0.86 using the 3D approach, compared with 0.72 for the 2D L3-based measurement. Similarly, psoas muscle volume showed excellent reliability (ICC(3,1)=0.94), exceeding that of psoas muscle cross-sectional area (ICC(3,1)=0.87).

The biomarkers showed strong agreement with the manually contoured test set. For lumbar vertebral bone density, mean absolute error (MAE) ranged from

Table 1. Reliability metrics for 2D and 3D psoas muscle biomarkers

Biomarker (T1 vs. T2)	**ICC (3,1)**	**95% CI**
3D psoas muscle density mean	0.86†	[0.75, 0.92]
2D psoas muscle density mean*	0.72†	[0.53, 0.84]
Psoas muscle volume	0.94†	[0.89, 0.97]
Psoas muscle cross-sectional area (CSA)*	0.87†	[0.77, 0.93]

* Measurement taken at the L3 vertebral body centroid.
† Statistically significant agreement ($p < 0.0001$).

8.24 to 15.01 HU, with R^2 values between 0.874 and 0.986 (Table 2). For muscle biomarkers, the MAE in psoas muscle density mean was 1.6 HU ($R^2 = 0.955$), and the MAE in psoas muscle volume was 9.79 cm^3 ($R^2 = 0.830$) (Table 3).

Table 2. Performance metrics for measurement of lumbar vertebral body density

Metric	**L1**	**L2**	**L3**	**L4**	**L5**
MAE	8.24 (HU)	15.01 (HU)	12.65 (HU)	14.90 (HU)	13.80 (HU)
R^2	0.986	0.908	0.954	0.874	0.976
SEM	2.46 (HU)	5.56 (HU)	4.68 (HU)	6.98 (HU)	3.78 (HU)

Table 3. Performance metrics for measurement of psoas muscle density and volume

Metric	**Psoas density mean**	**Psoas volume**
MAE	1.6 (HU)	9.79 (cm^3)
R^2	0.955	0.830
SEM	0.27 (HU)	1.15 (cm^3)

3.2 Longitudinal association with metastatic involvement

Table 4 summarizes associations from the mixed-effects models between imaging biomarkers and metastatic burden. Across all models, lower muscle and bone biomarker values were associated with higher metastatic burden ($p < 0.05$). In the univariable muscle models, both lower psoas muscle density ($\beta = -0.779$) and lower psoas muscle volume ($\beta = -0.816$) showed the strongest individual associations with metastatic burden, with comparable explanatory performance (marginal $R^2 = 0.415$ and 0.407, respectively). When combined, muscle density and volume remained independently associated with metastatic burden ($\beta = -0.561$ and $\beta = -0.507$, respectively), with a modest improvement in model fit (marginal $R^2 = 0.424$, conditional $R^2 = 0.861$).

Table 4. Associations between imaging biomarkers and metastatic burden.

Model	Coefficient β (SE)	Marginal R^2	Conditional R^2
Muscle density only	-0.779 (0.028)	0.415	0.855
Muscle volume only	-0.816 (0.032)	0.407	0.854
Combined muscle	muscle density: -0.561 (0.031) muscle volume: -0.507 (0.035)	0.424	0.861
Bone density only	-0.316 (0.024)	0.359	0.829
Bone and muscle	muscle density: -0.172 (0.025) muscle volume: -0.187 (0.026) bone density: -0.147 (0.028)	0.366	0.839

* All fixed-effect coefficients shown were statistically significant ($p < 0.05$).

Bone density was also associated with metastatic burden ($\beta = -0.316$), although the bone-only model explained less variance (marginal $R^2 = 0.359$) than the muscle-based models. In the combined bone and muscle model, all biomarkers remained significantly associated with metastatic burden, although the magnitude of their associations was reduced compared to the single-biomarker models. This suggests that muscle and bone biomarkers capture overlapping but complementary aspects of disease burden. Overall, muscle biomarkers showed the strongest associations with metastatic burden, while bone density remained an independent correlate in the joint model.

4 Discussion & Conclusion

We present a fully automated pipeline that quantifies longitudinal changes in MSK health from serial abdominal CT images. The pipeline integrates deep learning-based vertebrae detection with 3D vertebral body and psoas segmentation and cropping to anatomically standardized regions of interest, enabling consistent volumetric analysis across time points and producing robust 3D biomarkers. The proposed volumetric approach demonstrated low scan-to-scan variability in short-interval examinations and agreement with manual assessments of volumes of interest and biomarkers. Post hoc power analysis supported the adequacy of the quality-control sample size, as the standard error of measurement (SEM; Tables 2 and 3) was small relative to both the MAE and clinically meaningful biomarker differences. The principal innovation of this work lies in demonstrating state-of-the-art repeatability of 3D imaging biomarkers for tracking subtle, progressive MSK changes over time, thereby addressing a key limitation of prior single-time-point 2D approaches. The improved reliability may reflect reduced sensitivity to image plane location and patient positioning.

In advanced prostate cancer, regular abdominal imaging, prolonged survival, and development of osteosarcopenia are common. As such, imaging biomarkers may facilitate early identification of patients at risk for osteosarcopenia, treatment-related decline, and mortality. In this work, longitudinal biomarker changes were associated with metastatic involvement in advanced prostate can-

cer. In a separate study, we showed that these biomarkers were associated with fracture incidence in a younger (<55 years) subset of these patients, supporting their prognostic value. Future work will evaluate fracture risk prediction [21]. Integration of these biomarkers into predictive models could further enhance clinical decision support and guide timely therapeutic interventions.

Several limitations should be considered. Users of the proposed pipeline may need to normalize images or ensure that acquisition parameters are uniform. Differences in X-ray spectra across kVp settings may affect radiological density (HU) [22], although volumetric measurements are expected to be less sensitive. Restricting analysis to a single vendor (GE) and kVp (84% of scans) did not alter study results. Slice-thickness variations (1–5 mm) are also expected to have modest effects, as measurements are performed over large volumes (spanning many slices). Although this was a single-institution study, prior application of the pipeline to radiotherapy treatment-planning CT scans [23] and ongoing external validation on datasets from two partner institutions support its generalizability.

Given the growing recognition of osteosarcopenia as an important determinant of patient outcomes and quality of life, systematic monitoring of MSK health may yield useful, meaningful clinical data [24]. With continued advances in cancer treatment, patients are living longer, increasing the importance of monitoring disease and treatment-related MSK decline [25]. By enabling robust, opportunistic longitudinal monitoring from routinely acquired CT imaging, the proposed framework provides a practical means to quantify temporal changes in MSK health in patients with prostate and other cancers.

Acknowledgments. This work was supported by the Canadian Institutes of Health Research (CIHR) Project Grant (Application No. 452060), the SCACE Graduate Fellowship in Prostate Cancer Research, and the Hold'em for Life Oncology Fellowship.

Disclosure of Interests. The authors have no conflicts of interest.

References

1. Chen, S., Xu, X., Gong, H., et al.: Global epidemiological features and impact of osteosarcopenia: A comprehensive meta-analysis and systematic review. J. Cachexia Sarcopenia Muscle **15**(1), 8–20 (2024). https://doi.org/10.1002/jcsm.13392
2. Kirk, B., Zanker, J., Duque, G.: Osteosarcopenia: epidemiology, diagnosis, and treatment—facts and numbers. J. Cachexia Sarcopenia Muscle **11**(3), 609–618 (2020). https://doi.org/10.1002/jcsm.12567
3. Lee, A., McArthur, C., Ioannidis, G., et al.: Associations between osteosarcopenia and falls, fractures, and frailty in older adults. J. Am. Med. Dir. Assoc. **25**(1), 167–176 (2024). https://doi.org/10.1016/j.jamda.2023.09.027
4. Solla-Suarez, P., Arif, S.G., Ahmad, F., et al.: Osteosarcopenia and mortality in older adults undergoing transcatheter aortic valve replacement. JAMA Cardiol. **9**(7), 611–618 (2024). https://doi.org/10.1001/jamacardio.2024.0911
5. Stelmach-Mardas, M., Warchol, W., Garczyk, A., et al.: Influence of androgen deprivation therapy on the development of sarcopenia in patients with prostate cancer. Nutrients **16**(5), 656 (2024). https://doi.org/10.3390/nu16050656

6. Mazziotti, G., Lania, A.G., Laganà, M., Berruti, A.: Prediction of fragility fractures in men with prostate cancer under androgen deprivation therapy: The importance of a multidisciplinary approach using a mini-invasive diagnostic tool. Endocrine **83**(3), 594–596 (2024). https://doi.org/10.1007/s12020-023-03613-2
7. Smith, M.R., Finkelstein, J.S., McGovern, F.J., Zietman, A.L., Fallon, M.A., Schoenfeld, D.A., Kantoff, P.W.: Changes in body composition during androgen deprivation therapy for prostate cancer. J. Clin. Endocrinol. Metab. **87**(2), 599–603 (2002)
8. Greenspan, S.L., Nelson, J.B., Trump, D.L., Resnick, N.M.: Effect of once-weekly oral alendronate on bone loss in men receiving androgen deprivation therapy for prostate cancer. J. Clin. Endocrinol. Metab. **90**(12), 6410–6417 (2005)
9. Choi, W., Kim, C.H., Yoo, H., Yun, H.R., Kim, D.W., Kim, J.W.: Development and validation of a reliable method for automated measurements of psoas muscle volume in CT scans using deep learning-based segmentation: A cross-sectional study. BMJ Open **14**(5), e079417 (2024)
10. Rozynek, M., et al.: Use of artificial intelligence in the imaging of sarcopenia: A narrative review of current status and perspectives. Insights Imaging **12**, 160 (2021)
11. Beetz, N.L., Maier, C., Shnayien, S., et al.: Artificial intelligence-based analysis of body composition in Marfan: Skeletal muscle density and psoas muscle index predict aortic enlargement. J. Cachexia Sarcopenia Muscle **12**(4), 993–999 (2021)
12. Lee, S., et al.: Development of a fully automatic deep learning system for L3 selection and body composition assessment on computed tomography. Sci. Rep. **11**, 21656 (2021)
13. Deshpande, N., Hadi, M.S., Lillard, J.C., et al.: Alternatives to DEXA for the assessment of bone density: A systematic review. J. Neurosurg. Spine **38**(4), 436–445 (2023). https://doi.org/10.3171/2022.11.SPINE22875
14. Jain, R.K., Vokes, T.: Dual-energy X-ray absorptiometry. J. Clin. Densitom. **20**(3), 291–303 (2017). https://doi.org/10.1016/j.jocd.2017.06.014
15. Hofmann, F.O., Heiliger, C., Tschaidse, T., Jarmusch, S., Auhage, L.A., Aghamaliyev, U., Gesenhues, A.B., Schiergens, T.S., Niess, H., Ilmer, M., Werner, J.: Validation of body composition parameters extracted via deep learning-based segmentation from routine computed tomographies. Sci. Rep. **15**(1), 11909 (2025)
16. Klein, G., Hardisty, M., Whyne, C., Martel, A.L.: VertDetect: Fully end-to-end 3D vertebral instance segmentation model. arXiv:2311.09958 (2023)
17. Klein, G., et al.: Metastatic vertebrae segmentation for use in a clinical pipeline. In: International Workshop and Challenge on Computational Methods and Clinical Applications for Spine Imaging, pp. 123–132. Springer, Cham (2019)
18. Wasserthal, J., Breit, H.-C., Meyer, M.T., Pradella, M., Hinck, D., Sauter, A.W., Heye, T., Boll, D., Cyriac, J., Yang, S., Bach, M., Segeroth, M.: TotalSegmentator: Robust segmentation of 104 anatomic structures in CT images. Radiol. Artif. Intell. **5**(5), e230024 (2023). https://doi.org/10.1148/ryai.230024
19. Sekuboyina, A., Husseini, M.E., Bayat, A., et al.: VerSe: A vertebrae labelling and segmentation benchmark for multi-detector CT images. arXiv:2001.09193 (2020)
20. Löffler, M.T., Sekuboyina, A., Jacob, A., et al.: A vertebral segmentation dataset with fracture grading. Radiol. Artif. Intell. **2**(4), e190138 (2020). https://doi.org/10.1148/ryai.2020190138
21. Ross, T., et al.: Quantifying bone health in metastatic prostate cancer patients diagnosed under 55 with opportunistic cancer surveillance screening. Orthop. Proc. **108**(SUPP_2) (2026)

22. Nhila, O., et al.: Evaluation of CT acquisition protocols effect on Hounsfield units and optimization of CT-RED calibration curve selection in radiotherapy treatment planning systems. Moscow Univ. Phys. Bull. **77**(4), 661–671 (2022)
23. Castaño Sainz, Y., Chen, S., Tabatabaei, S., Ross, T.D., Whyne, C., Detsky, J., Sahgal, A., Hardisty, M.: Characterization of osteosarcopenia in spinal metastases patients to be treated with stereotactic body radiotherapy using quantitative image-based AI-derived biomarkers. In: Proc. 12th Int. Conf. Bioinformatics Research and Applications (ICBRA), pp. 27–32 (2025)
24. Loncar, G., Cvetinovic, N., Lainscak, M., et al.: Bone in heart failure. J. Cachexia Sarcopenia Muscle **11**(2), 381–393 (2020). https://doi.org/10.1002/jcsm.12516
25. Yang, F., et al.: Association of sex, age, and Eastern Cooperative Oncology Group performance status with survival benefit of cancer immunotherapy in randomized clinical trials: A systematic review and meta-analysis. JAMA Netw. Open **3**(8), e2012534 (2020)